Applied Surface Science 318 (2014) 142–149

Contents lists available at ScienceDirect

Applied Surface Science

journal homepage: www.elsevier.com/locate/apsusc

# $TiO_2$–$Al_2O_3$ binary mixed oxide surfaces for photocatalytic $NO_x$ abatement

Asli Melike Soylu[a], Meryem Polat[a], Deniz Altunoz Erdogan[a], Zafer Say[a], Cansu Yıldırım[b], Özgür Birer[b,c], Emrah Ozensoy[a,*]

[a] Department of Chemistry, Bilkent University, 06800 Ankara, Turkey
[b] KUYTAM Surface Science and Technology Center, Koç University, 34450 Istanbul, Turkey
[c] Department of Chemistry, Koç University, 34450 Istanbul, Turkey

ARTICLE INFO

*Article history:*
Received 15 November 2013
Received in revised form 10 February 2014
Accepted 12 February 2014
Available online 22 February 2014

*Keywords:*
$TiO_2$
$Al_2O_3$
Photocatalysis
$NO_x$ abatement
$DeNO_x$

ABSTRACT

$TiO_2$–$Al_2O_3$ binary oxide surfaces were utilized in order to develop an alternative photocatalytic $NO_x$ abatement approach, where $TiO_2$ sites were used for ambient photocatalytic oxidation of NO with $O_2$ and alumina sites were exploited for $NO_x$ storage. Chemical, crystallographic and electronic structure of the $TiO_2$–$Al_2O_3$ binary oxide surfaces were characterized (via BET surface area measurements, XRD, Raman spectroscopy and DR-UV-Vis Spectroscopy) as a function of the $TiO_2$ loading in the mixture as well as the calcination temperature used in the synthesis protocol. 0.5 Ti/Al-900 photocatalyst showed remarkable photocatalytic $NO_x$ oxidation and storage performance, which was found to be much superior to that of a Degussa P25 industrial benchmark photocatalyst (i.e. 160% higher $NO_x$ storage and 55% lower $NO_2$(g) release to the atmosphere). Our results indicate that the onset of the photocatalytic $NO_x$ abatement activity is concomitant to the switch between amorphous to a crystalline phase with an electronic band gap within 3.05–3.10 eV; where the most active photocatalyst revealed predominantly rutile phase together and anatase as the minority phase.



## 1. Introduction

Indoor and outdoor air pollutants such as $NO_x$, $SO_x$, volatile organic compounds (VOCs) and particulate matter (PM) result in significantly adverse effects on human health. Further negative implications of air pollution can also be observed on water resources, agriculture and biological habitat [1–6]. Among these airborne toxic species, particularly nitrogen oxides ($NO_x$) present a major challenge for air purification. $NO_x$ species (i.e. mostly NO(g), $NO_2$(g) and $N_2O$(g)) are generated during the fossil fuel combustion processes via the homogenous reaction of nitrogen and oxygen gases at high temperatures where the major contribution comes from NO(g). $NO_x$ abatement can be performed in a very efficient manner using thermal catalytic technologies such as selective catalytic reduction (SCR) [7–9] and $NO_x$ storage and reduction (NSR) (which is also called Lean $NO_x$ Traps, LNT) [10–12] at elevated temperatures (i.e. $T > 300\,^{\circ}C$). In these thermally activated catalytic $DeNO_x$ technologies although SCR approach requires utilization of urea as an external reducing agent, NSR/LNT technology can be used in the absence of an additional reducing agent. However, an important challenge in air purification is the abatement of gaseous $NO_x$ species under ambient conditions (i.e. at room temperature and under regular atmospheric conditions). Photocatalytic systems offer promising opportunities in order to tackle this important environmental challenge, as these systems can be tailored to efficiently clean/purify air under ambient conditions with the help of ultraviolet (UV) and/or visible (VIS) light [13]. Among these systems $TiO_2$-based materials are the most effective photocatalysts for air/water purification applications [14,15]. However it has been reported that complete photocatalytic reduction of toxic $NO_x$ species into harmless $N_2$ occurs only with a relatively limited performance for these systems [13].

In the current work, rather than attempting to perform complete photocatalytic reduction of $NO_x$, an alternative $NO_x$ abatement strategy has been demonstrated, which includes photocatalytic oxidation of $NO_x$ on a $TiO_2$/$Al_2O_3$ binary oxide photocatalyst surface and its *storage in the solid state* in the form of nitrates and nitrites. This alternative strategy was inspired by our recent studies on NSR technology which is used for the thermal catalytic after treatment of automotive $NO_x$ emissions [12,16–21]. In couple of these former studies, we spectroscopically demonstrated

* Corresponding author. Tel.: +90 312 290 2121; fax: +90 312 266 4068.
*E-mail address:* ozensoy@fen.bilkent.edu.tr (E. Ozensoy).
*URL:* http://www.fen.bilkent.edu.tr/ ozensoy (E. Ozensoy).

http://dx.doi.org/10.1016/j.apsusc.2014.02.065
0169-4332/

that [12,16–21] on the $TiO_2/Al_2O_3$ binary oxide surface, oxidized $NO_x$ species such as $NO_2(g)$ can readily undergo a thermal disproportionation reaction forming adsorbed nitrites and nitrates allowing effective solid state $NO_x$ storage. However NO(g) has a limited adsorption energy on many metal oxide surfaces compared to that of $NO_2$, hindering the storage of NO in the solid (adsorbed) state. Thus, for solid state $NO_x$ storage, NO should be first oxidized to $NO_2$ and then subsequently stored on the available adsorption sites of the catalyst surface in the form of nitrites/nitrates. Although this can be done readily at elevated temperatures using a platinum group metal (PGM) promoted metal oxide catalyst such as $Pt/Al_2O_3$, it cannot be efficiently achieved under ambient conditions (i.e. at room temperature) due to kinetic limitations. However this limitation can be overcome by designing a catalytic system including a photocatalytic NO(g) oxidation component which is coupled to a $NO_x$ storage component. Along these lines, in the current work, we show that $TiO_2/Al_2O_3$ binary oxide surfaces can be exploited to perform photocatalytic $NO_x$ oxidation and storage, where $TiO_2$ surface domains provide NO oxidation capability under ambient conditions, converting $NO(g) + O_2(g)$ into nitrites/nitrates while the high-surface area $Al_2O_3$ component enables both the dispersion of the photocatalytic $TiO_2$ domains as well as the creation of additional storage sites for oxidized $NO_x$. Once saturated with $NO_x$, such a photocatalytic $NO_x$ oxidation and storage catalyst can readily be regenerated by treatment with water, which can dissolve the adsorbed nitrites/nitrates and restore the $NO_x$ adsorption sites [22].

In order to demonstrate this alternative strategy, in the current study, a set of $TiO_2/Al_2O_3$ binary oxide photocatalysts were synthesized and characterized. A sol–gel synthesis method was used to co-precipitate titania with alumina. The influences of the surface structure on the photocatalytic NO oxidation and storage was investigated by modifying the surface structure via calcination. Photocatalytic performances of this new family of $TiO_2/Al_2O_3$ binary oxide photocatalysts were also compared with a commercially available photocatalyst (i.e. Degussa P25) in order to determine the relative performance of the $TiO_2/Al_2O_3$ system against a widely used industrial benchmark.

## 2. Experimental

### 2.1. Sample preparation

Titanium (IV) isopropoxide (TIP, 97%, Sigma–Aldrich) and aluminum-tri-*sec*-butoxide (ASB, 97%, Sigma–Aldrich) were used as the main ingredients in the preparation of the $TiO_2/Al_2O_3$ binary oxides via sol–gel method [16,18]. Three series of samples were prepared by varying the relative molar composition of the $TiO_2$ component in the $TiO_2/Al_2O_3$ binary oxide. These samples are labeled as "*x*Ti/Al-*y*", where *x* represents the $TiO_2$ to $Al_2O_3$ mole ratio (i.e. 0.25, 0.5 and 1.0) and *y* represents the calcination temperature (150–1000 °C) of the sample. In the synthesis, depending on the corresponding $TiO_2$–$Al_2O_3$ mole ratio, an appropriate amount of ASB was mixed with propan-2-ol (99.5%, Sigma–Aldrich) and acetylacetone (99.3%, Fluka) for 30 min. Subsequently, TIP was added in a drop wise fashion to the mixture over the course of another 30 min. All of the synthesis steps were carried out at room temperature under vigorous stirring. The co-precipitation of the obtained hydroxides was accomplished after the gradual addition of 0.5 M $HNO_3$(aq) to the solution which led to the formation of a gel. The resulting yellow gel was aged under ambient conditions for 2 days and the dried sample was ground to form a fine powder. Next, synthesized $TiO_2/Al_2O_3$ binary oxides were calcined in air for 2 h at various temperatures ranging from 150 to 1000 °C.

### 2.2. Structural characterization measurements

Determination of the crystal structure of the synthesized materials were carried out with a Rigaku Miniflex X-ray diffractometer (XRD) equipped with Cu Kα radiation operated at 30 kV, 15 mA, and 1.54 Å (wavelength of copper X-ray source). The XRD patterns were recorded in the $2\theta$ range of 10–60° with a step width of 0.02 $s^{-1}$. Raman spectra of the samples were collected in the range of 200–1500 $cm^{-1}$ with a resolution of 4 $cm^{-1}$ using a Horiba Jobin Yvon LabRAM HR800 spectrometer equipped with a confocal Raman BX41 microscope. The Raman spectrometer was equipped with a Nd:YAG laser ($\lambda$ = 532.1 nm) where the laser power was 20 mW. The specific surface area (SSA) values of the $TiO_2$ samples were determined by conventional Brunauer–Emmett–Teller (BET) $N_2$ adsorption method using a Micromeritics Tristar 3000 surface area and pore size analyzer. Prior to the BET measurements, all of the samples were outgassed in vacuum for 2 h at 150 °C. Diffuse Reflectance UV–vis (DR-UV–vis) spectra were utilized in order to obtain electronic band gap values. These spectra were recorded with a Shimadzu UV-3600 UV-Vis-NIR spectrophotometer using the ISR-3100 integrating sphere attachment in the specular reflection (8°) mode. Barium sulfate ($BaSO_4$) was used as the reference material in the DR-UV–vis measurements. Obtained DR-UV–vis spectra were finally corrected using the Kubelka-Munk transformation.

### 2.3. Photocatalytic activity measurements

The custom-designed photocatalytic flow reactor system (Scheme 1) was used to measure the photocatalytic $NO_x$ oxidation and storage performances of $TiO_2/Al_2O_3$ binary oxides under UVA excitation. The photocatalytic flow reactor system mainly consisted of a gas manifold system, a sample compartment and a chemiluminiscence $NO_x$ analyzer (Horiba APNA-370). The gas manifold system was connected to gas cylinders containing $N_2(g)$ (99.998%, Linde GmbH), $O_2(g)$ (99.998%, Linde GmbH) and 100 ppm NO diluted in $N_2$ (Linde GmbH). Mass flow controllers (MFCs, MKS 1479A) were used to control the volumetric flow rates of gases and a capacitance pressure gauge (MKS Baratron) was used to measure total pressure of the flowing gas which was set to 1 atm. The following flow rates were used to prepare the gas mixture, 0.750 SLM (standard liters per minute) for $N_2(g)$, 0.250 SLM for $O_2(g)$, and 0.010 SLM for NO(g) with a total gas flow rate of 1.010 SLM. Prior to mixing, $N_2(g)$ and $O_2(g)$ were also bubbled through a humidifier. The relative humidity of the total gas mixture was 70% RH which was measured with a Hanna HI 9565 humidity analyzer at the sample position in the photocatalytic flow reactor. This gas mixture represents a synthetic polluted air sample. Before the performance tests, synthesized powder samples were placed on a 2 mm × 40 mm × 40 mm polymethyl methacrylate (PMMA) sample holder and subsequently irradiated with UVA (350 nm) light bulbs (F8W/T5/BL350, Sylvania/Germany) under ambient conditions for 18 h outside the flow reactor in order to remove the surface contaminations and to activate the photocatalysts. For each measurement, typically a 950 mg activated photocatalyst sample was placed into the flow reactor. The photocatalytic flow reactor was illuminated with 8W UVA lamps (F8W/T5/BL350, Sylvania/Germany) whose emission wavelength was 350 nm. Concentrations of NO(g), $NO_2(g)$ and total $NO_x(g)$ species in the photocatalytic reactor were quantitatively measured online with the chemiluminiscence $NO_x$ analyzer.

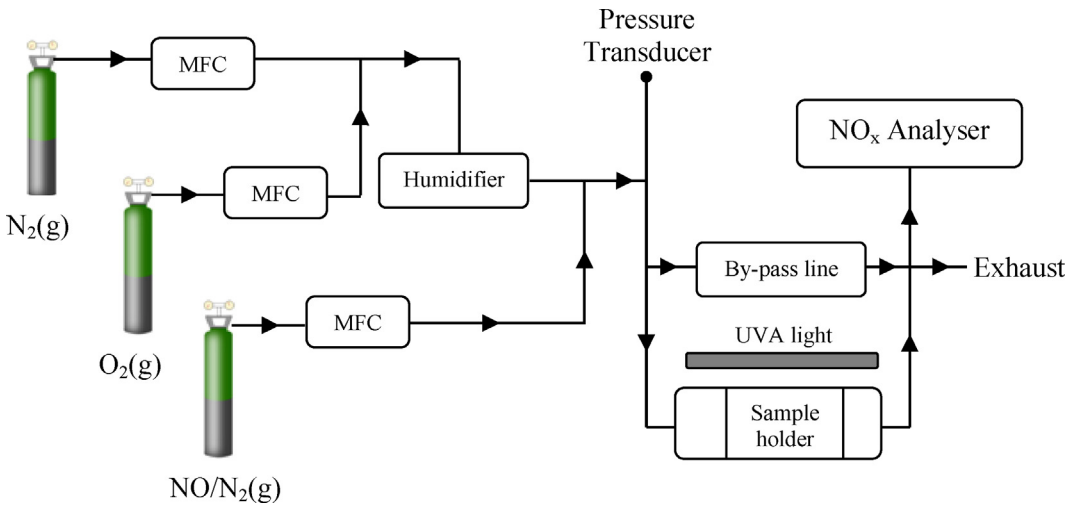


**Scheme 1.** Description of the custom-designed photocatalytic flow reactor system.

Gas phase photocatalytic activity measurements are reported in terms of per cent photonic efficiencies ($\zeta\%$) as described in Eqs. (1) and (2).

$$\zeta\% = \frac{n_{NO_x}}{n_{photon}} \times 100 \quad (1)$$

where $n_{NO_x}$ corresponds to either the decrease in the total number of moles of all gaseous $NO_x$ species or the number of moles of $NO_2$(g) generated in a 60 min (i.e. 3600 s) photocatalytic performance test. On the other hand, $n_{photon}$ corresponds to the total number of incident UVA photons impinging on the catalyst surface in 3600 s, which can be calculated through Eq. (2) as:

$$n_{photon} = \frac{I\lambda St}{Nhc} \quad (2)$$

where $I$ represents the photon power density of the UVA lamp, experimentally measured at the sample position in the photocatalytic reactor (typically, 7.5 W m$^{-2}$), $\lambda$ is the representative emission wavelength of the UVA lamp (i.e. 350 nm), $S$ is the surface area of the photocatalyst sample holder in the reactor that is exposed to the UVA irradiation (i.e. 40 mm × 40 mm = 1600 mm$^2$); $t$ is the duration of the performance test (i.e. 3600 s), $N$ is the Avogadro's number, $h$ is Planck's constant and $c$ is the speed of light.

## 3. Results and discussion

### 3.1. Specific surface area measurements

Thermal evolution and the structural variations of the $TiO_2/Al_2O_3$ binary oxide samples with varying molar compositions were investigated after calcination steps at different temperatures (Fig. 1). Fig. 1 reveals that $TiO_2/Al_2O_3$ samples possessed a relatively high surface area after preparation and calcination at low temperatures (e.g. ≥420 m$^2$/g). These high SSA values were preserved to a large extent up to 600 °C. This observation is in very good accordance with the current XRD and Raman results (Figs. 2 and 3) suggesting a predominantly amorphous structure for all $TiO_2/Al_2O_3$ binary oxide samples below 600 °C. At higher temperatures, a drastic and a monotonic decrease in the SSA values were observed in line with the enhanced crystallinity and structural ordering of the samples at elevated temperatures which are also evident in the current XRD and Raman measurements (Figs. 2 and 3). It is worth mentioning that upon calcination at 900 °C, SSA values for 0.25Ti/Al-900, 0.5Ti/Al-900, 1.0Ti/Al-900 samples decreased to 108, 64 and 25 m$^2$/g, respectively. These particular values are rather close to the SSA of the commercial Degussa P25 catalyst (i.e. 55 m$^2$/g) which is used as the benchmark photocatalyst in the current study. At higher calcination temperatures such as 1000 °C, SSA values for all of the $TiO_2/Al_2O_3$ binary oxide samples drastically decrease to c.a. 9–17 m$^2$/g which is in perfect agreement with the increased crystallinity and the formation of the low surface area phases such as rutile and $\alpha$-$Al_2O_3$ (corundum) observed in the XRD and Raman experiments (Figs. 2 and 3).

### 3.2. XRD and Raman spectroscopy experiments

Fig. 2 presents XRD profiles obtained for the $TiO_2/Al_2O_3$ samples with different molar compositions that were calcined at various temperatures within 150–1000 °C. It is apparent that for all samples, calcination at temperatures less than or equal to 600 °C yields amorphous structures. Calcination at 800 °C results in the first discernible indications of crystallinity, where $\gamma$-$Al_2O_3$ (JCPDS 29-0063) phase starts to be visible for 0.25 Ti/Al and 0.5Ti/Al samples. For the 1.0 Ti/Al sample, in addition to the $\gamma$-$Al_2O_3$ phase, formation of anatase (JCPDS 21-1272) and rutile (JCPDS 04-0551) phases of $TiO_2$ also becomes visible. It is clear that with increasing $TiO_2$ to $Al_2O_3$ mole ratio in the photocatalyst composition, crystallinity of

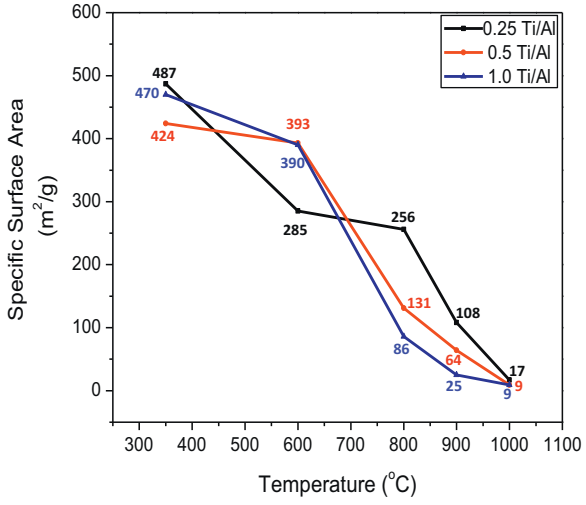


**Fig. 1.** Specific surface area values for the $TiO_2/Al_2O_3$ binary oxide samples with different molar compositions that were calcined at various temperatures within 150–1000 °C in air.

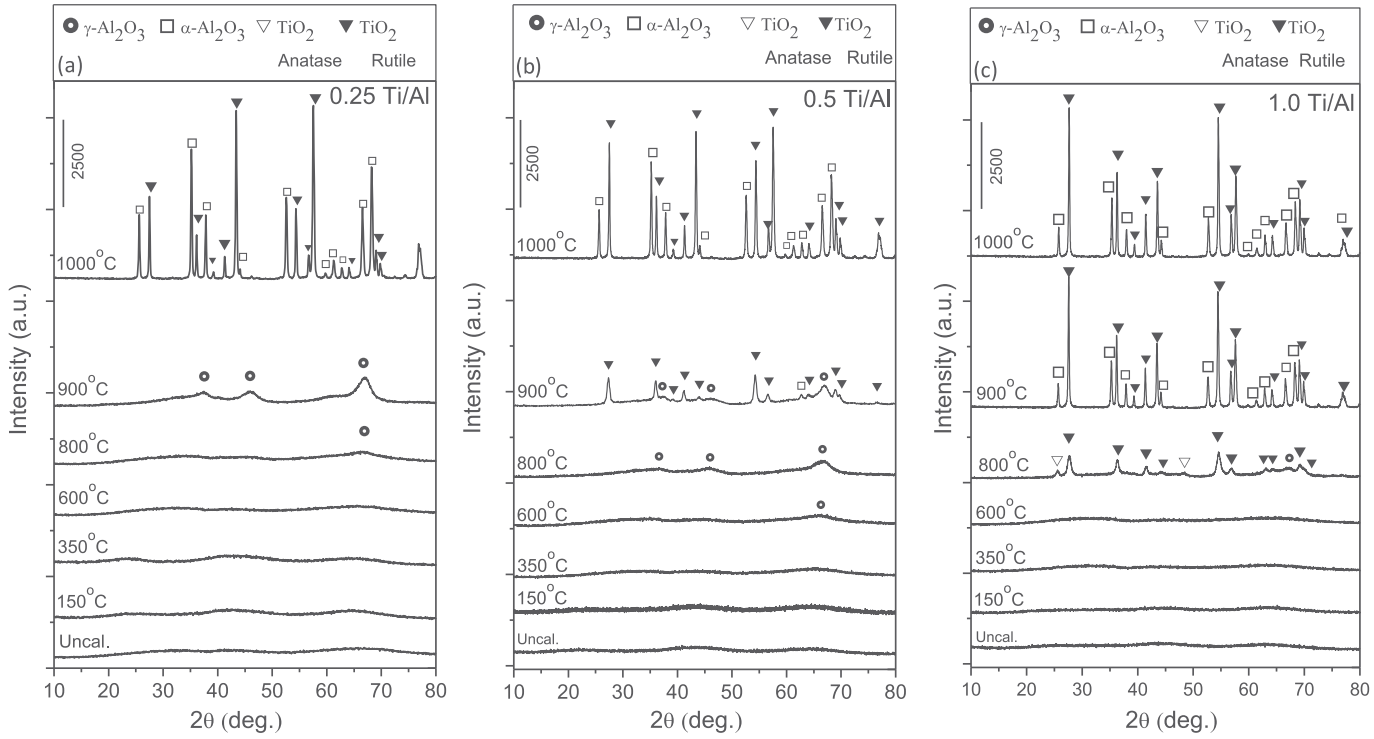


**Fig. 2.** XRD patterns for the $TiO_2/Al_2O_3$ binary oxide samples with different molar compositions that were calcined at various temperatures within 150–1000 °C in air.

the observed phases increases. This is in line with the fact that pure (bulk) $TiO_2$ has much lower phase transition temperatures between amorphous, anatase and rutile phases than the $TiO_2$ domains on the $TiO_2/Al_2O_3$ surface [16,18]. Thus at low $TiO_2$ to $Al_2O_3$ mole ratios, there exists a strong interaction between the $TiO_2$ minority domains and the $Al_2O_3$ majority domains, which is decreasing the surface mobility of the $TiO_2$ domains and hindering the nucleation and growth of anatase and rutile phases at low temperatures. However at higher $TiO_2$ to $Al_2O_3$ mole ratios, interaction between the $TiO_2$ and $Al_2O_3$ domains weakens to a certain extent as $TiO_2$ converges to a more bulk-like configuration, pushing the phase transition temperatures to lower (bulk-like) values.

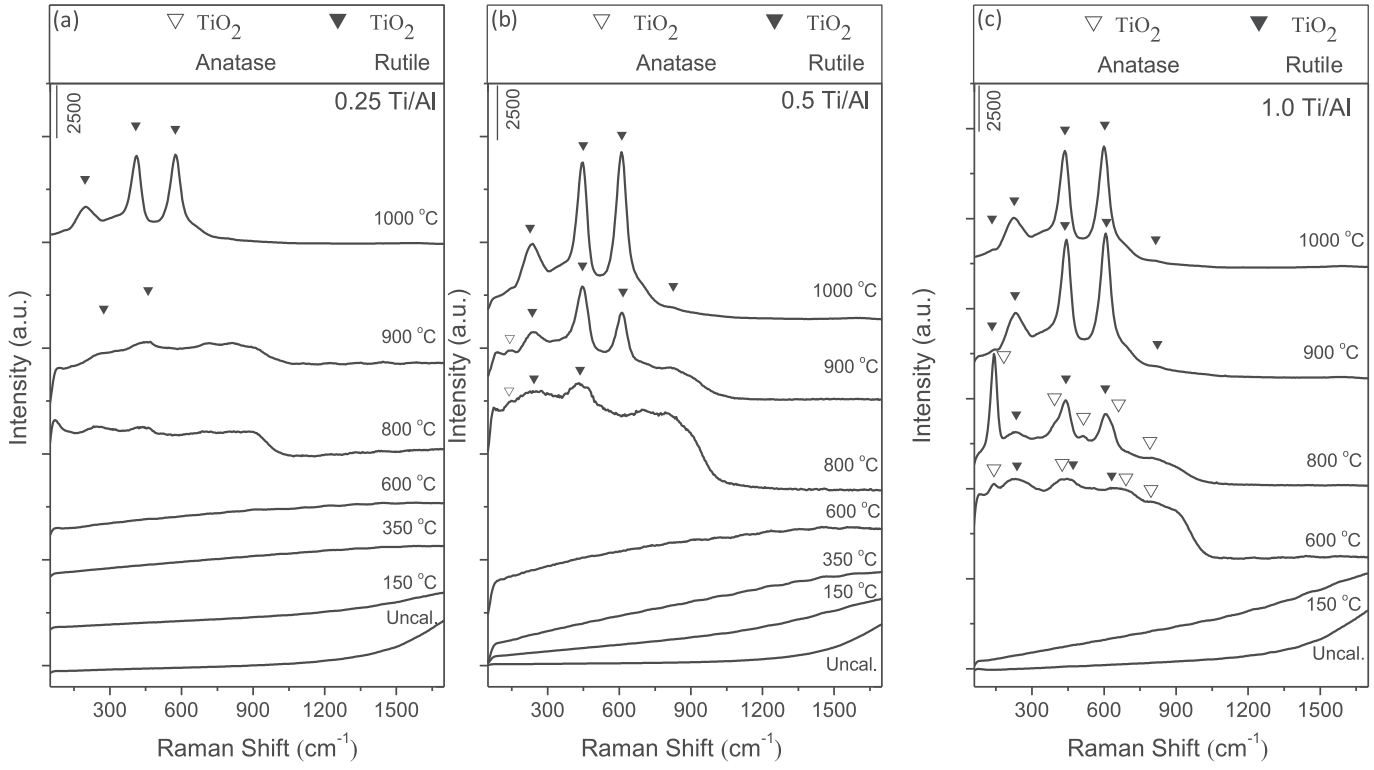


**Fig. 3.** Raman spectra for the $TiO_2/Al_2O_3$ binary oxide samples with different molar compositions that were calcined at various temperatures within 150–1000 °C in air.

Upon calcination at 900 °C, although γ-$Al_2O_3$ seems to be the only discernible crystalline phase on the 0.25 Ti/Al surface (where $TiO_2$ is still in amorphous state), anatase and rutile phases become clearly visible on the 0.5 Ti/Al and 1.0 Ti/Al surfaces where the crystallinity of the latter is significantly greater. This is in perfect agreement with the SSA values presented in Fig. 1, suggesting a much lower SSA for the 1.0 Ti/Al-900 sample compared to 0.25 Ti/Al-900 and 0.5 Ti/Al-900 samples. It is also worth mentioning that although α-$Al_2O_3$ (JCPDS 10-0173) phase is not significantly visible at 900 °C for lower $TiO_2$ to $Al_2O_3$ mole ratios; this phase is noticeably discernible for the 1.0 Ti/Al-900 sample. Furthermore, α-$Al_2O_3$ (corundum) phase starts to appear during the anatase to rutile phase transition. As discussed in one of our former reports [16], this can be explained by the formation of a solid solution between anatase and alumina. In this solid solution, when the anatase phase is converted into rutile at elevated temperatures, a phase segregation occurs which triggers a phase transition in the alumina component from γ to α-phase. Finally, after calcination at 1000 °C, all samples seem to be highly ordered, where corundum and rutile are the only visible crystalline phases, in very good harmony with the drastic SSA decreases observed for these samples in Fig. 1.

Raman spectra of the synthesized $TiO_2/Al_2O_3$ binary oxide samples with different molar compositions that were calcined at various temperatures within 150–1000 °C are given in Fig. 3. These Raman spectral features can be readily explained in the light of the XRD results given in Fig. 2, as well as the former Raman spectroscopic studies in the literature [16,18,23,24]. It is known that the Raman spectrum of anatase phase shows six Raman features ($1A_{1g}$, $2B_{1g}$, and $3E_g$) at 144 ($E_g$), 197 ($E_g$), 399 ($B_{1g}$), 516 ($A_{1g}+B_{1g}$), 639 ($E_g$) and 796 $cm^{-1}$ ($E_g$) [23]. On the other hand, the rutile phase can be characterized by a Raman spectrum with four major Raman active features ($A_{1g}+B_{1g}+B_{2g}+E_g$) at 143 ($B_{1g}$), 447 ($E_g$), 612 ($A_{1g}$), 826 $cm^{-1}$ ($B_{2g}$) and also a two-phonon scattering band at 236 $cm^{-1}$ [24]. In very good agreement with the XRD results given in Fig. 2, up to 600 °C, all samples reveal an amorphous structure with no sharp Raman features. It is worth mentioning that sample 1.0 Ti/Al-600 reveals very broad and convoluted Raman signals corresponding to small and poorly crystalline anatase and rutile domains which seem to be elusive to detect in XRD (Fig. 2c). At calcination temperatures higher than 600 °C, anatase phase appears as the dominant phase together with a minor contribution from rutile. With increasing temperature, anatase to rutile ratio in the samples decreases where at 900 °C rutile becomes the predominant phase detected in the Raman spectra. For the 0.5 Ti/Al-900 sample, anatase phase is still visible in the Raman spectra (Fig. 3b), although rutile is definitely the majority phase. In perfect harmony with the XRD results (Fig. 2), Raman spectra in Fig. 3 also suggest that increasing $TiO_2$ to $Al_2O_3$ mole ratio enhances the crystallinity of the phases on the $TiO_2/Al_2O_3$ binary oxide surfaces which is evident by the sharper and stronger Raman scattering features.

### 3.3. Photocatalytic performance experiments

Fig. 4 shows a typical concentration versus time plot that is obtained during a photocatalytic performance test. In Fig. 4, the total $NO_x$ concentration (i.e. sum of the concentrations of all of the $NO_x$ species existing in the reactor, i.e. blue curve) as well as separate NO(g) (black curve) and $NO_2$(g) (red curve) concentrations in the photocatalytic reactor measured by the chemiluminiscence $NO_x$ analyzer are presented. During the initial c.a. 20 min of the analysis, a synthetic polluted air gas mixture comprised of $N_2$(g), $O_2$(g), $H_2O$(g) as well as 1 ppm NO(g) is fed to the photocatalyst surface under dark conditions where the UVA lamp is off and any background exposure to sunlight is prevented. Under these conditions (i.e. in the first 15 min), a minor transient fall in the total $NO_x$(g) and NO(g) concentrations was observed. This can be attributed to the dilution of the gas in the reactor pipeline and the thermal adsorption of $NO_x$ species on the gas lines, reactor walls as well as adsorption on the photocatalyst surface. Since the reactor is kept in complete darkness under these conditions, no photocatalytic activity is observed during this initial stage evident by the presence of a minor amount of $NO_2$(g) production due to thermal catalytic disproportionation processes occurring on the catalyst surface. Following this initial transient period, reactor walls and the photocatalyst surface are saturated with $NO_x$, after which $NO_x$(g) and NO(g) traces quickly return to the original inlet concentration value of c.a. 1 ppm, signifying the end of thermal catalytic activity.

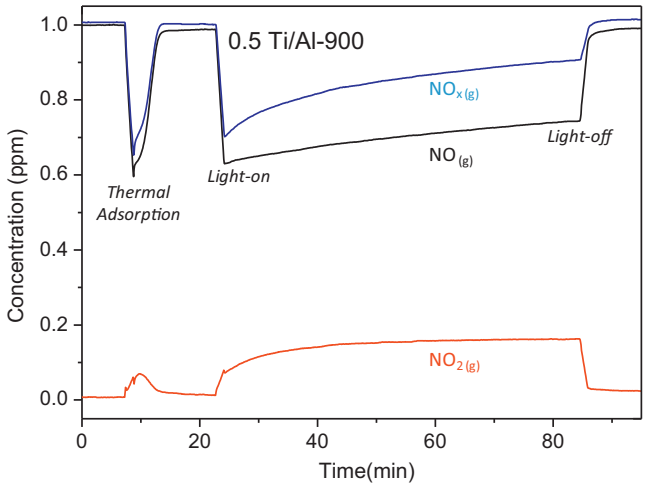


**Fig. 4.** Concentration versus time plot for the photocatalytic performance test of the 0.5 Ti/Al-900 sample. Blue, black and red curves correspond to the concentrations of total $NO_x$(g), NO(g) and $NO_2$(g), respectively (see text for details). (For interpretation of the references to color in this figure legend, the reader is referred to the web version of this article.)

After this preliminary transient period, UVA excitation source is turned on and the photocatalytic reaction is started. Upon UVA illumination, a drastic and a permanent fall in the NO(g) and total $NO_x$(g) concentrations concomitant to a quick and significant jump in the $NO_2$(g) level, were observed. This behavior suggests the conversion of NO(g) into $NO_2$(g) via photocatalytic oxidation. Furthermore, produced $NO_2$(g) can adsorb on the photocatalyst surface in the form of chemisorbed $NO_2$, nitrites and nitrates [16,18] and stored in the solid state, resulting in a further fall in the NO(g) and total $NO_x$ signals. It is worth mentioning that, fall in the NO(g) concentration might also have some contribution from the direct photocatalytic decomposition and photo-reduction of NO(g) forming $N_2$(g) and/or $N_2O$(g) [25]. However, since the direct photocatalytic reduction is known to be a relatively inefficient pathway, this reaction channel may be expected to be a minor photochemical route. Consequently, the total $NO_x$ concentration (blue) curve (which is mostly comprised of the sum of NO(g) and $NO_2$(g) signals) in Fig. 4 remains mostly below 1 ppm during the UVA-activated regime, illustrating the continuous photocatalytic activity and $NO_x$ storage in the solid state.

Photochemical NO oxidation and storage performance tests were performed for all of the synthesized samples and the summary of these performance tests were presented in terms of percent photonic efficiencies in Fig. 5, along with the corresponding data for the Degussa P25 industrial benchmark. In the histogram given in Fig. 5, blue and red bars represent the percent photonic efficiencies for total $NO_x$(g) decrease and $NO_2$(g) production, respectively. These values were obtained by integrating the corresponding areas under the concentration versus time curves for the data similar to the ones given in Fig. 4.

It is worth mentioning that for an ideal catalyst with an utmost photocatalytic $DeNO_x$ performance, blue bars (i.e. $NO_x(g)$ storage/conversion) should be maximized; while red bars are simultaneously minimized (i.e. minimum slip of toxic $NO_2(g)$ into the atmosphere). When the behavior of the Degussa P25 industrial benchmark photocatalyst given in Fig. 5 is investigated, it is immediately seen that this industrial photocatalyst has a very high NO(g) photo-oxidation capability generating a large quantity of $NO_2(g)$, while the same catalyst has a very limited $NO_x$ storage capability (blue bar). Considering the fact that $NO_2(g)$ is a much more toxic pollutant than NO(g), although Degussa P25 industrial benchmark system is very active in photo-oxidation, this material does not qualify to be a very efficient photocatalytic $DeNO_x$ system for $NO_x$ abatement. Another benchmark sample used in the control experiments was $\gamma$-$Al_2O_3$. Fig. 5 unambiguously indicates that, $\gamma$-$Al_2O_3$ has neither significant photocatalytic $NO_x$ storage nor photocatalytic $NO_2(g)$ production capabilities.

On the other hand, when the photocatalytic performance data for the $TiO_2/Al_2O_3$ binary oxide samples are examined, one can immediately note the remarkable improvement in the photocatalytic $DeNO_x$ performance compared to the Degussa P25 industrial benchmark. In Fig. 5, performance results for the $TiO_2/Al_2O_3$ binary oxide samples are assembled in three groups based on $TiO_2$ to $Al_2O_3$ mole ratio (i.e. 0.25, 0.5 and 1.0) in the photocatalyst structure. It is visible that for the 0.25 Ti/Al samples calcined at various temperatures, catalysts calcined below 900 °C reveal very low $DeNO_x$ performance, where the performance reaches an optimum value between 900 and 950 °C and starts to fall at 1000 °C.

A similar performance trend is observed for 0.5 Ti/Al catalysts calcined at various temperatures (Fig. 5). For this family of catalysts, although no significant activity is observed at calcination temperatures less than 900 °C, photocatalytic $DeNO_x$ performance presents a very radical enhancement at 900 °C, revealing values that are much better than any of the photocatalysts in the 0.25 Ti/Al family. It is worth mentioning that a further increase in the calcination temperature to 1000 °C results in the photocatalytic $DeNO_x$ performance of the 0.5 Ti/Al system.

Fig. 5 indicates that for the 1.0 Ti/Al photocatalyst family, no significant photocatalytic activity is detected up to 800 °C, while at this calcination temperature a remarkable increase in the activity is observed, though this catalyst is not as effective as the 05 Ti/Al-900 catalyst in total $NO_x$ abatement, due to the significant $NO_2(g)$ generation of the former. It can be seen in Fig. 5 that for calcination temperatures above 800 °C, $NO_x$ abatement starts to fall, evident by the increased $NO_2(g)$ slip into the atmosphere as well as decreasing $NO_x$ storage in the solid state. Thus, a general analysis of the performance results presented in Fig. 5 reveals that, 0.5 Ti/Al-900 binary oxide catalyst shows the highest $NO_x$ abatement performance among all of the analyzed photocatalysts, where it performs 160% higher $NO_x$ storage and 55% lower $NO_2(g)$ release to the atmosphere compared to the Degussa P25 industrial benchmark.

Photocatalytic performance of the $TiO_2/Al_2O_3$ binary oxide samples can be readily interpreted in the light of current structural characterization experiments (Figs. 1–3) which reveal valuable insight regarding the specific surface areas as well as the crystallographic phases that are present on the Ti/Al samples. Firstly, it is apparent in Fig. 5 that for the best performing photocatalyst family (i.e. 0.5 Ti/Al), onset of activity is observed in a very drastic manner as the calcination temperature is increased from 800 °C to 900 °C. BET, XRD and Raman measurements given in Figs. 1–3 suggests that this thermal window directly overlaps with the crystallization of the amorphous $TiO_2$ to form a mixture of anatase and rutile phases where the latter is the dominant phase. In other words, it is apparent that in order to achieve the best photocatalytic $NO_x$ abatement performance, a unique crystallographic mixture of anatase and rutile phases has to be obtained.

Secondly, Fig. 5 also suggests that for Ti/Al families with different $TiO_2$ loadings, ultimate performance is observed for the intermediate loading and the performance was seen to decrease for very low or very high $TiO_2$ loadings. This can be explained by the fact that at low $TiO_2$ loadings, it is likely that $TiO_2$ loading is not high enough to be dispersed on all of the $Al_2O_3$ surface. Thus not all of the $NO_x$ adsorption/storage (i.e. $Al_2O_3$) sites can be utilized due to limited photo-oxidation capability of the inadequate number of $TiO_2$ oxidation sites on the surface. On the other hand, at very high $TiO_2$ loadings, $TiO_2$ covers most of the $Al_2O_3$ surface and upon calcination above 800 °C, SSA of the catalyst sample falls drastically together with the formation of crystalline anatase and rutile mixture; limiting the available number of $NO_x$ storage sites that are available after photo-oxidation.

Thirdly, Fig. 5 indicates that onset of photocatalytic activity is observed in a rather sharp manner at 950, 900 and 800 °C for the 0.25Ti/Al, 0.5Ti/Al and 1.0Ti/Al samples, respectively. In

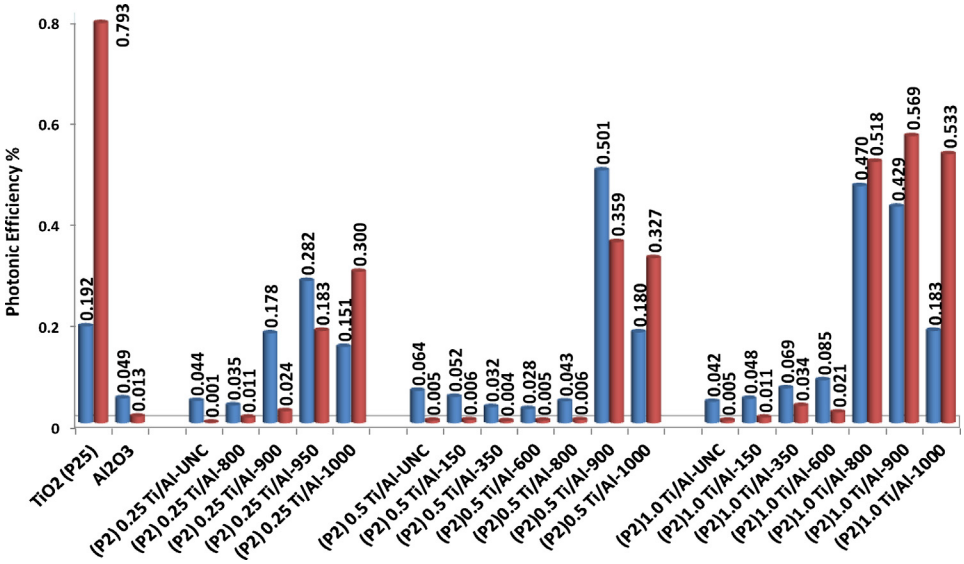


**Fig. 5.** Photocatalytic $DeNO_x$ performance results for the $TiO_2/Al_2O_3$ binary oxide samples with different molar compositions that were calcined at various temperatures within 150–1000 °C in air.

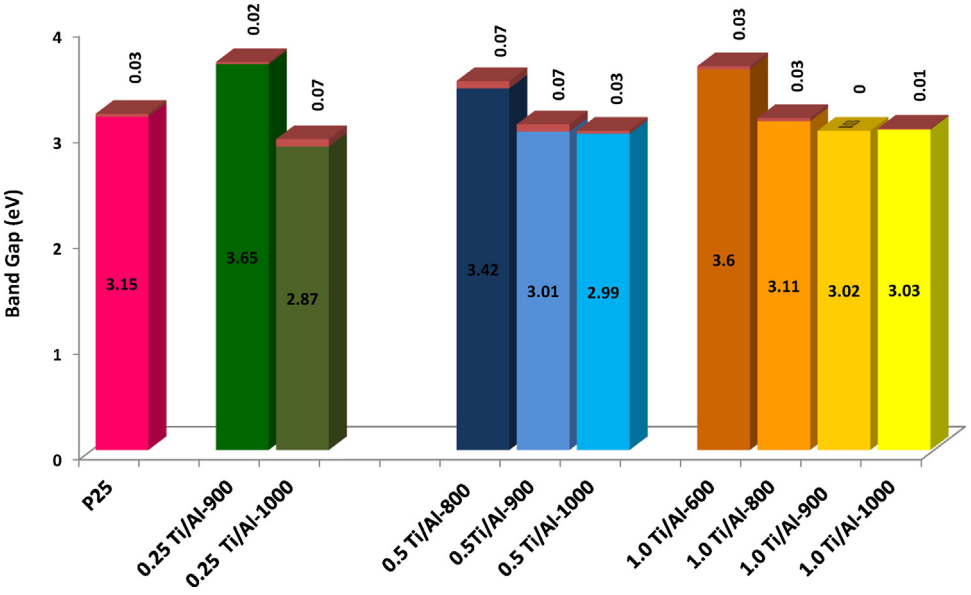


**Fig. 6.** Electronic band gap values derived from DR-UV–vis spectroscopic results for the $TiO_2/Al_2O_3$ binary oxide samples with different molar compositions that were calcined at various temperatures within 150–1000 °C in air.

other words, as the relative $TiO_2$ loading in the $TiO_2/Al_2O_3$ binary oxide samples increases, onset temperature for the photocatalytic activity shifts to lower temperatures. This can also be explained by the onset temperature for the crystallization of Ti/Al samples (and hence the formation of photo-active $TiO_2$ sites) observed in XRD and Raman measurements (Figs. 2 and 3) which suggest that increasing $TiO_2$ loading increases the temperature required to switch form an amorphous $TiO_2$ structure to a crystalline structure.

### 3.4. DR-UV–vis measurements and electronic band gap

In order to investigate the relationship between the electronic structure and the photocatalytic $NO_x$ abatement performance, electronic band gap values were calculated from the currently performed (not shown) DR-UV–vis spectroscopic measurements. These band gap values are presented in Fig. 6. In very good agreement with the discussion given above, electronic band gap values for the relatively inactive amorphous Ti/Al samples which are calcined at lower temperatures, reveal a characteristically high value within 3.4–3.6 eV. On the other hand, with the onset of the photocatalytic activity, a very sharp fall in the electronic band gap values were observed, where the band gap decreases to a typical value of 3.05–3.10 eV, in line with the formation of ordered anatase and rutile phases. Typical band gap values for bulk anatase and rutile phases are c.a. 3.2 and 3.0 eV, respectively [26]. Thus, for the active photocatalyst samples, the band gap value is in between that of anatase and rutile, being closer to the latter, in accordance with the fact that in the most active photocatalyst, rutile exists as the predominant phase together with anatase as the minority phase.

It is also worth noting that although onset of the photocatalytic activity as a function of calcination temperature can be followed with the electronic band gap values, electronic band gap cannot be used as a sole indicator for the estimation of the photocatalytic activity trends. This is due to the fact that once the photocatalytically active structure is obtained leading to a drastic decrease in the electronic band gap, band gap values cease to change at higher calcination temperatures although photocatalytic activity starts to decline.

## 4. Conclusions

$TiO_2$–$Al_2O_3$ binary oxide surfaces were utilized in order to develop an alternative photocatalytic $NO_x$ abatement approach, where $TiO_2$ sites were used for ambient photocatalytic oxidation of NO with $O_2$ and alumina sites were exploited for $NO_x$ storage. Chemical, crystallographic and electronic structure of the $TiO_2$–$Al_2O_3$ binary oxide surfaces were characterized as a function of the $TiO_2$ loading in the mixture as well as the calcination temperature used in the synthesis protocol. 0.5 Ti/Al-900 photocatalyst showed remarkable photocatalytic $NO_x$ oxidation and storage performance which was found to be much superior to that of a Degussa P25 industrial benchmark photocatalyst (i.e. 160% higher $NO_x$ storage and 55% lower $NO_2$(g) release to the atmosphere). Our results indicate that the onset of the photocatalytic for $NO_x$ abatement activity is concomitant to the switch between amorphous to a crystalline phase with an electronic band gap within 3.05–3.10 eV where the most active photocatalyst revealed predominantly rutile phase together with anatase as the minority phase.

## Acknowledgments

Authors acknowledge Zafer Say for performing BET measurements. E.O. also acknowledges financial support from Turkish Academy of Sciences through the “TUBA-GEBIP Outstanding Young Scientist Prize” and from Fevzi Akkaya Science Fund (FABED) through Eser Tümen Scientific Achievement Award as well as the Scientific and Technical Research Council of Turkey (TUBITAK) (Project Code: 109M713).

## References

[1] O. Carp, C.L. Huisman, A. Reller, Photoinduced reactivity of titanium dioxide, Prog. Solid State Chem. 32 (2004) 33–177.
[2] A.K. Gupta, K. Karar, S. Ayoob, K. John, Spatio-temporal characteristics of gaseous and particulate pollutants in an urban region of Kolkata, India, Atmos. Res. 87 (2008) 103–115.
[3] S. Ishii, J.N.B. Bell, F.M. Marshall, Phytotoxic risk assessment of ambient air pollution on agricultural crops in Selangor State, Malaysia, Environ. Pollut. 150 (2007) 267–279.

[4] R. Chen, B. Zhou, H. Kan, B. Zhao, Associations of particulate air pollution and daily mortality in 16 Chinese cities: an improved effect estimate after accounting for the indoor exposure to particles of outdoor origin, Environ. Pollut. 182 (2013) 278–282.
[5] Air Quality Guidelines for Europe, 2nd ed., World Health Organization Regional Office for Europe (WHO Regional Publications, European Series, No. 91), Copenhagen, 2000.
[6] Air quality and health, World Health Organization, Fact Sheet No: 313, Updated September 2011.
[7] R.M. Heck, Catalytic abatement of nitrogen oxides—stationary applications, Catal. Today 53 (1999) 519–523.
[8] Y. Traa, B. Burger, J. Weitkamp, Zeolite-based materials for the selective catalytic reduction of $NO_x$ with hydrocarbons, Microporous Mesoporous Mater. 30 (1998) 3–41.
[9] G. Busca, L. Lietti, G. Ramis, F. Berti, Chemical and mechanistic aspects of the selective catalytic reduction of $NO_x$ by ammonia over oxide catalysts: a review, Appl. Catal. B: Environ. 18 (1998) 1–36.
[10] W.S. Epling, L.E. Campbell, A. Yezerets, N.W. Currier, J.E. Parks II, Overview of the fundamental reactions and degradation mechanisms of $NO_x$ storage/reduction, Catal. Rev. Sci. Eng. 46 (2004) 163–245.
[11] S. Roy, A. Baiker, $NO_x$ storage-reduction catalysis: from mechanism and materials properties to storage-reduction performance, Chem. Rev. 109 (2009) 4054–4091.
[12] E. Ozensoy, J. Szanyi, C.H.F. Peden, Model $NO_x$ storage systems: storage capacity and thermal aging of $BaO/\theta\text{-}Al_2O_3/NiAl(1\,0\,0)$, J. Catal. 243 (2006) 149–157.
[13] J. Lasek, Y.H. Yu, J.C.S. Wu, Removal of $NO_x$ by photocatalytic processes, J. Photochem. Photobiol. C: Photochem. Rev. 14 (2013) 29–52.
[14] V. Loddo, G. Marci, C. Martin, L. Palmisano, V. Rives, A. Sclafani, Preparation and characterisation of $TiO_2$ (anatase) supported on $TiO_2$ (rutile) catalysts employed for 4-nitrophenol photodegradation in aqueous medium and comparison with $TiO_2$ (anatase) supported on $Al_2O_3$, Appl. Catal. B: Environ. 20 (1999) 29–45.
[15] A. Mitsionis, T. Vaimakis, C. Trapalis, N. Todorova, D. Bahnemann, R. Dillert, Hydroxyapatite/titanium dioxide nanocomposite for controlled photocatalytic $NO_x$ oxidation, Appl. Catal. B: Environ. 106 (2011) 398–404.
[16] S.M. Andonova, G.S. Senturk, E. Kayhan, E. Ozensoy, Nature of the Ti–Ba interactions on the $BaO/TiO_2/Al_2O_3$ $NO_x$ storage system, J. Phys. Chem. C 113 (2009) 11014–11026.
[17] E. Kayhan, S.M. Andonova, G.S. Senturk, C.C. Chusuei, E. Ozensoy, Fe promoted $NO_x$ storage materials: structural properties and $NO_x$ uptake, J. Phys. Chem. C 114 (2010) 357–369.
[18] S.M. Andonova, G.S. Senturk, E. Ozensoy, Fine-tuning the dispersion and the mobility of BaO domains on $NO_x$ storage materials via $TiO_2$ anchoring sites, J. Phys. Chem. C 114 (2010) 17003–17016.
[19] E. Emmez, E.I. Vovk, V.I. Bukhtiyarov, E. Ozensoy, Direct evidence for the instability and deactivation of mixed-oxide systems: influence of surface segregation and subsurface diffusion, J. Phys. Chem. C 115 (2011) 22438–22443.
[20] E.I. Vovk, E. Emmez, M. Erbudak, V.I. Bukhtiyarov, E. Ozensoy, Role of the exposed Pt active sites and $BaO_2$ formation in $NO_x$ storage reduction systems: a model catalyst study on $BaO_x/Pt(1\,1\,1)$, J. Phys. Chem. C 115 (2011) 24256–24266.
[21] G.S. Senturk, E.I. Vovk, V.I. Zaikovskii, Z. Say, A.M. Soylu, V.I. Bukhtiyarov, E. Ozensoy, $SO_x$ uptake and release properties of $TiO_2/Al_2O_3$ and $BaO/TiO_2/Al_2O_3$ mixed oxide, systems as $NO_x$ storage materials, Catal. Today 184 (2012) 54–71.
[22] Soylu, Polat, Ozensoy manuscript, in preparation.
[23] T. Ohsaka, F. Izumi, Y. Fujiki, Raman spectrum of anatase $TiO_2$, J. Raman Spectrosc. 7 (1978) 321–324.
[24] H.L. Ma, J.Y. Yang, Y. Dai, Y.B. Zhang, B. Lu, G.H. Ma, Raman study of phase transformation of $TiO_2$ rutile single crystal irradiated by infrared femtosecond laser, Appl. Surf. Sci. 253 (2007) 7497–7500.
[25] O. Carp, C.L. Huisman, A. Reller, Photoinduced reactivity of titanium dioxide, Prog. Solid State Chem. 32 (2004) 33–177.
[26] D.A.H. Hanaor, C.C. Sorrell, Review of the anatase to rutile phase transformation, J. Mater. Sci. 46 (2011) 855–874.